Check for updates

Solar hydrogen production: a bottom-up analysis of different photovoltaic–electrolysis pathways

M. Reuß, [ID] *[a] J. Reul,[a] T. Grube, [ID] [a] M. Langemann,[a] S. Calnan, [ID] [b] M. Robinius, [ID] [a] R. Schlatmann,[b] U. Rau [ID] [c] and D. Stolten [ID] [ad]

The conventional energy system is undergoing a transformation towards renewable energy technologies, as society strives for sustainable and green energy supply. This has created challenges, such as spatial and temporal imbalances of energy demand and feed-in arising from volatile renewable energy resources. A possible solution to this challenge is presented by hydrogen as a versatile chemical storage medium. Promising technologies for producing hydrogen from renewable energy include the production pathways photoelectrolysis (PEC) and photovoltaic–electrolysis (PV–EL). This paper examines three production pathways which differ in the connection and integration of the constituent photovoltaic (PV) and electrolysis (EL) subsystems by modelling the integrated system's behaviour under the various device designs and operational conditions. The model is based on the electrochemical processes and addresses losses and how the overall performance can be enhanced, in contrast to literature-based models. The efficiency of the subsystems, as well as the coupling efficiency, are predicted under various conditions, enabling the determination of optimum design and operational parameters. This analysis is enhanced by an application of the PV–EL pathways to the hourly weather conditions of Jülich, Germany. The solar to hydrogen efficiency was found to drop as the level of integration increased. The study showed that varying weather conditions strongly affect the efficiency of integrated systems and should be further taken into account for future improvement and cost estimations of integrated device performance.

1 Introduction

Impending challenges such as climate change, air pollution, and decreasing fossil resources are shifting the conventional energy system towards the implementation of renewable energy technologies. A future energy system, based on renewables, is dependent on the fluctuating and locally-dispersed availability of solar, wind and water resources.[1,2] The deployment of hydrogen as a versatile energy carrier for future energy concepts would enable temporal imbalances within the energy supply to be corrected.[3–6] Solar-driven electrolysis constitutes a promising option of generating hydrogen from renewable resources.[7] Past research has revealed two promising pathways of solar hydrogen generation, namely: photoelectrochemical (PEC)[8] and photovoltaic–electrolytic (PV–EL)[9] water splitting. Both concepts combine the photovoltaic effect with electrolysis to convert sunlight into hydrogen. The difference between the two approaches is in the degree of integration of the subsystems.[10]

[a] Forschungszentrum Jülich GmbH, IEK-3: Institute of Electrochemical Process Engineering, D-52425 Jülich, Germany. E-mail: m.reuss@fz-juelich.de

[b] PVcomB, Helmholtz Zentrum Berlin für Materialen und Energie GmbH, Schwarzschildstraße 3, D-12489 Berlin, Germany

[c] Forschungszentrum Jülich GmbH, IEK-5: Photovoltaics, D-52425 Jülich, Germany

[d] RWTH Aachen University, Chair for Fuel Cells, Faculty of Mechanical Engineering, Kackertstraße 9, D-52072 Aachen, Germany

Jacobsson *et al.*[11] describe the transition from PEC to PV–EL in seven different device configurations, (a) to (g), in a highly comprehensible manner, as visualized in Fig. 1.

The PEC combines the photovoltaic effect and electrolysis within a single device, directly coupling them but unlike PV solar cells, light is absorbed by a photoelectrode which generates carriers that are separated by a potential formed at a junction with an electrolyte at which also the water splitting occurs. The photoelectrode consists of either a single semi-conductor solar cell or a multi-junction device, whose bandgap or the sum of band gaps, respectively exceeds the water splitting potential. The single-junction approach to generating hydrogen without an external power source, using titanium dioxide (TiO_2) and platinum (Pt), was first demonstrated by Fujishima and Honda[12] in 1972, building the basis for the research field of photoelectrochemical water splitting. Despite numerous modifications to the original device, such as the employment of other semi-conducting materials[13,14] or catalysts,[15,16] metal loading[17] and doping,[18–20] solar-to-hydrogen (STH) efficiencies have remained limited and below 5%.[13,14,16,21–25] Because of these efficiency restrictions, contemporary research focuses on multi-junction devices with optimised adaption to solar light and the potential requirements for water splitting. These devices achieve STH efficiencies η_{STH} of up to 15%[26–28] and provide the possibility for upscaling to larger areas.[29]
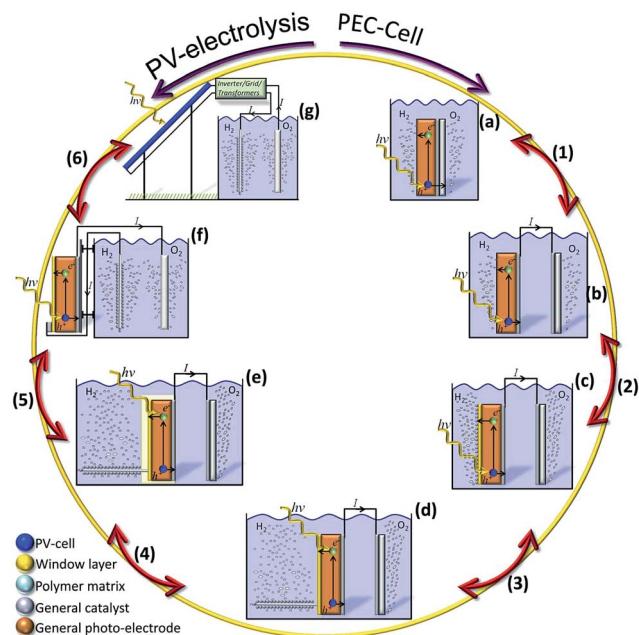
Fig. 1 Illustration of a gradual transition in six steps from a monolithic PEC device (a), to a free-standing electrolyzer connected to a PV cell (g) (reproduced from Jacobsson et al.[11] with permission from The Royal Society of Chemistry).

Conversely for the PV–EL pathway, the photogenerated carriers are separated by a semiconductor–semiconductor (both solid) junction and are transported, usually *via* wires, to a separate solid–liquid junction where the water splitting by electrolysis takes place. Typically PV–EL pathway incorporates commercial PV modules and electrolysers that are either directly coupled or connected *via* a converter.[11,30] Laboratory-scale devices have already achieved STH-efficiencies greater of than 18%.[31,32] Jia *et al.*[33] have proven an STH efficiency of over 30% by deploying a highly efficient but non-commercial triple-junction III–V-solar cell. The theoretical STH efficiency limit of PV–EL systems can be estimated from by the individual energy conversion efficiencies of the PV and EL subsystems. Assuming a laboratory-scale record power conversion efficiency (PCE) of 46% (ref. 34) and an electrolysis efficiency of 90%, the theoretical η_{STH} limit could reach approximately 41% emphasising the future potential of PV–EL hydrogen production pathways. As already reviewed by Jacobsson *et al.*,[11] hybrid devices incorporating both the PEC and PV–EL concepts in one device are possible and have been demonstrated on a laboratory scale.

Research within the field of solar hydrogen production focuses on two approaches. On the one side, practical fundamental research is undertaken, that aims to maximise the η_{STH} for the various experimental PEC and PV–EL laboratory setups. On the other hand, the potential and operational behaviour of these devices as approximated by models. These can be further distinguished into large-scale, top-down models,[35–37] based on literature and empirical efficiencies, and bottom-up models,[38–43] based on the physical and chemical principles of the subsystems and their interaction. Below we recount representative studies in the past used to estimate the cost of hydrogen

production based on the top-down models and then on the bottom-up models.

Shaner *et al.*[44] conducted an economic assessment of hydrogen production pathways in which the costs of hydrogen production were calculated and compared for two approaches for each of the pathways, PEC (1 sun and concentrated solar) and PV–EL (grid-connected *vs.* island). All pathways are modelled with a fixed STH efficiency of 9.8%, except for a prospective PEC-approach with STH efficiency of 20%. Sathre *et al.*[45] estimated the net energy performance of a potential large-scale PEC facility considering both mass and energy balances, assuming three different scenarios for the STH efficiency of 5%, 10% and 20% from a heuristic perspective. Meanwhile, Pinaud *et al.*[46] analysed the costs of hydrogen production by photoelectrolysis *via* different PEC configurations for immersed particle bed systems and panel based immersed PV systems using the then state of the art performance of the different system components. For most of these studies it was concluded that the hydrogen production costs were dominated by the device η_{STH}[45,46] and additionally depending on the configuration by the device lifetime[45] or balance of system costs.[44]

The complementary bottom-up approaches deploy variable models to describe the behaviour of the PV and EL subsystems as a function of the input parameters irradiation, cell, and ambient temperature. Atlam *et al.*[10] described an optimal sizing method for an electrolyser within a directly coupled PV–EL pathway based on a linear approximation of the PV and EL subsystems. Garcia-Valverde *et al.*[47,48] optimised the coupling of the PV and EL subsystems for three different configurations by mapping the maximum power points (MPP) of the PV in a cloud and matching the electrolysis characteristics to this cloud of MPPs. Sayedin *et al.*[38,49–51] optimised the correlation of the PV and EL subsystem by deploying different methods, such as particle swarm and multi-objective non-linear optimisation. These optimisation approaches for directly coupled PV–EL systems were augmented by the analysis of practically optimised systems.[39,40] Clarke *et al.*[42] tested a PV–EL system that consisted of a 2.4 kW polycrystalline PV-array and a PEM electrolyser for an operational duration of 60 days. These previous studies aimed at finding the matching point between the PV and EL components, but typical field operation occurs far from the optimum working point.

The focus of the present contribution is on analysing the reasons for coupling losses and less on finding the optimum operating conditions and design parameters for the PV and EL subsystems to minimise the coupling losses. Additionally, the efficiencies of the PV and EL subsystems are investigated under operating conditions in which both, irradiation and ambient temperature, fluctuate similar to Pinaud *et al.*[46] This makes this model applicable to dynamic input data and thus delivers insight into operational behaviour under real conditions. Furthermore, this work examines the local integration of the subsystems into a single device as well as the related implications for energy conversion efficiency to hydrogen.

Therefore, the present work was aimed at providing a broad bottom-up modelling tool for solar hydrogen production, based

on performance characteristics derived from experimentally observed physical and chemical processes, to complement existing modelling approaches. This model is expected to aid decision-making in the choice of the diverse solar-to-hydrogen pathways and their applications by estimating their hydrogen production.

The modelling tool contains three PV–EL concept alternatives, with differences regarding the integration and coupling of the subsystems as well as a modelling approach for a PEC device. A detailed analysis of the model will be given in the next section. The subsystems were composed of devices with the respective state-of-the-art technology, such that the modelling considered a silicon heterojunction (SHJ) solar-cell on the PV-side and a PEM electrolysis-stack on the EL-side. The model-behaviour is analysed in dependence of design- and operating-parameters. As a final step, the model is applied on meteorological data for Jülich, Germany, to showcase the applicability to real world conditions.

2 Methods and assumptions

The previous section described the hydrogen production pathways of PEC and PV–EL that consist of the two main subsystems, the PV and the EL compartment. The individual modelling approaches for these subsystems are outlined in this section before the interaction of the subsystems within the overall system of a solar-to-hydrogen pathway is discussed.

The data that is used within to model the PV-module corresponds to the VBHN330SA15 series from Panasonic derived from the SAM database.[52] The chosen module is also available on the European market as the VBHN330SJ47 series and employs the *silicon heterojunction (SHJ)* technology. SHJ currently constitutes the PV-technology with the highest commercially available Power Conversion Efficiency (PCE).[53,54] The PCE of this specific module is 19.7% under 1.5 AM illumination. Table 1 lists the module parameters.

The maximum power point MPP defines the optimum operating point of the PV module and is used to define the PCE of the device at standard test conditions (AM1.5 global irradiation, module temperature of 25 °C). The PCE represents the proportion of incident photon energy that is converted to electrical energy and is given by the product of U_{MPP} and I_{MPP} divided by the product of incident irradiation G and the total
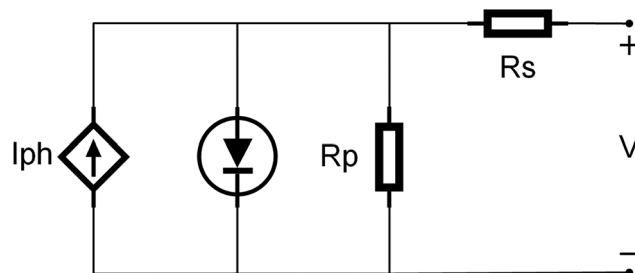

Fig. 2 Equivalent electrical circuit of the one-diode-model for a PV module.[55]

area of the PV module. The current–voltage behaviour of the PV module under varying operational parameters, such as ambient temperature and solar irradiation is approximated by the one-diode model represented by the equivalent electrical circuit shown in Fig. 2. This circuit consists of a current source, providing a photocurrent I_{ph} whose related power output at the device terminals is reduced by several parasitic components:

(i) Recombination losses represented by a diode reverse saturation current I_0 flowing through a non-ideal diode with a modified ideality factor a, in parallel with the photocurrent source

(ii) an ohmic resistance R_P parallel to the photocurrent source through which current losses through shunts occur

(iii) a series resistance R_S which causes voltage losses *via* the terminal current I flowing through it.

De Soto *et al.*[56] developed a system of equations based on five parameters to describe this circuit. The primary equation is given as eqn (1):

$$I = I_{ph} - I_0 \left[e^{\frac{U+IR_S}{a}} - 1 \right] - \frac{U + IR_S}{R_p} \tag{1}$$

With the modified ideality factor a, defined in eqn (2):

$$a = \frac{N_s n k T_c}{e} \tag{2}$$

To estimate the temperature of the PV cells, the "Normal Operating Cell Temperature" T_{NOCT} approach was chosen.[56] The five reference parameters, as well as T_{NOCT} of the selected PV module, are listed in Table 2.

Fig. 3 shows the results of the one-diode model in comparison to the parameters at short circuit, open circuit, maximum power point and at NOCT conditions, from the module datasheet. The U–I behaviour, as well as the temperature dependencies of the PV module, are obviously well represented by the model which indicates the correct implementation of the approach of De Soto *et al.*[56]

The modelling of the electrolysis is based upon the characteristic polarisation curve, which depicts the dependency between the current density j and voltage U.[57–59] The U–j-curve of PEM electrolysis is comprised of the Nernst potential, activation and ohmic overpotentials, as well as the concentration losses.

Table 1 Performance parameters of the VBHN330SA15 series PV module from Panasonic[52]

Parameter		Value	Unit
P_{MPP}	Power at MPP	330.6	[W]
U_{MPP}	Voltage at MPP	58.0	[V]
I_{MPP}	Current at MPP	5.7	[A]
U_{OC}	Open circuit voltage	69.7	[V]
β_{VOC}	Temperature coefficient for open circuit voltage	−0.170	[V °C^{-1}]
I_{SC}	Short circuit current	6.1	[A]
α_{ISC}	Temperature coefficient for short circuit current	0.002	[A °C^{-1}]

Table 2 Reference input parameters for one-diode model approach, extracted from SAM database[52] for the selected Panasonic PV Module VBHN330SJ47

Parameter		Value	Unit
$R_{S,ref}$	Series resistance	0.741	[Ohm]
$R_{P,ref}$	Ohmic resistance	457.17	[Ohm]
a_{ref}	Ideality factor	2.3402	
$I_{ph,ref}$	Photo current	6.08	[A]
$I_{0,ref}$	Saturation current	6.88×10^{-13}	[A]
T_{NOCT}	Normal operating cell temperature	43.8	[°C]

$$U_{cell} = U_{Nernst} + U_{act} + U_{Ohm} + U_{conc} \tag{3}$$

The open circuit voltage is given by the Nernst equation, which considers effects due to deviations of pressure and temperature from standard conditions (25 °C, 1 atm).

$$U_{Nernst} = U_0 - \frac{RT}{zF} \sum \vartheta_i \ln(a_i(T)) \tag{4}$$

The valence z is two for water electrolysis and a_i is the activity. The standard potential is determined with the free enthalpy of the reaction at standard conditions.

$$U_0 = \frac{\Delta G^0}{-zF} = 1.185 \text{ V} \tag{5}$$

The activation and ohmic overpotentials are determined with the eqn (6) and (7):

$$U_{act} = \alpha \times \ln\left(\frac{j}{j_0(T)}\right) \tag{6}$$

$$U_{Ohm} = j \times (R_{ion}(T) + R_{ele} + R_{cont}) \tag{7}$$

These overpotentials are dependent on the properties of the catalytic materials, pressure and cell temperature. The factors α and j_0 have to be derived from experimental results. In this work, these parameters are drawn from Tjarks,[57] who measured a PEM electrolysis cell under different pressure and temperature conditions. The ionic resistance R_{ion} is a function of the temperature, while the electric R_{ele} and contact resistances R_{cont} are constant values. The values of $R_{ele} = 0.096 \Omega$ and $R_{cont} = 0.025 \Omega$ can be found in literature.[57] The concentration losses are neglected, as they only occur at high current densities, due to insufficient supply of reactant gases. Based on these adjustments, the cell voltage U_{cell} is derived as follows:

$$U_{cell} = 1.185 \text{ V} - \alpha(T) \times \ln\left(\frac{j}{j_0(T)}\right) + j \times (R_{ion}(T) + 0.025 \ \Omega + 0.096 \ \Omega) \tag{8}$$

The remaining temperature-dependent variables are $\alpha(T)$, $j_0(T)$ and $R_{ion}(T)$. The respective values are drawn from Tjarks.[57] Faradaic losses are neglected in this analysis, as the electrolysis
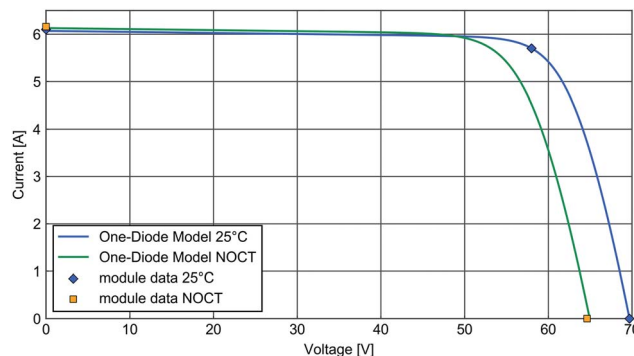

Fig. 3 Comparison of current–voltage curves (lines) derived using the one-diode model[56] with performance parameters (symbols) derived from the module data sheet.

system is assumed to be operated under atmospheric conditions. The operational limit is addressed by curtailment in case of excess voltage above the nominal system voltage in order to avoid increased cell decay. The pathways, which incorporate power electronics, decrease the power supply to the electrolyser to the maximum voltage input. If there is no converter between the PV and EL subsystem, the power supply is cut to zero if the excess input voltage exceeds voltages of 5% above the nominal voltage input.

Fig. 4 shows the resulting polarisation curves of the electrolysis model in comparison to the data measured by Tjarks.[57]

The cell efficiency of the electrolyser is then calculated using the cell voltage:[60]

$$\eta_{EL,cell} = \frac{H_u}{2 \times e \times N_A \times U_{cell}} \tag{9}$$

The current $I_{EL,stack}$ of the electrolyser is determined by the product of the current density j and the active electrode area A_{EL}. This area is determined within the design phase of each pathway and can be optimised, depending on the location-
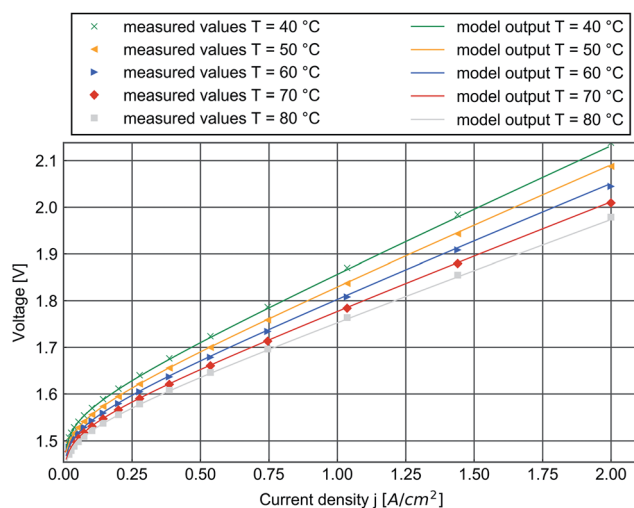

Fig. 4 Polarisation curves of the electrolysis for different operating temperatures T_{OP} in comparison to measured values from Tjarks.[57]

specific solar irradiation and the power characteristics of the employed PV subsystem.

$$I_{EL,stack} = j_{EL,cell} \times A_{EL} \qquad (10)$$

Depending on which hydrogen production pathway is considered, the interaction and coupling of the PV and EL subsystems differ. This work considers three different integration steps, whereas the thermally and electrically-coupled consideration is investigated for two different operating temperatures. These four pathways are portrayed in Fig. 5 and outlined in the following.

The PV–EL I operates with PV and EL compartments that are locally separated and electrically connected by a converter. With regard to Fig. 1, from Jacobsson et al.,[11] this setup is referred to as design (g). The separation of PV and electrolysis enables the use of commercially-available PV modules and electrolysers. The converter module adjusts the PV-output to the demanded EL input parameters. An advantage of the converter is that there are no coupling losses apart from those related to the converter efficiency. The assumed behaviour of converter efficiency as a function of partial loading is shown in Fig. 6 and represents a typical converter behaviour from the SAM database.[52] The assumed converter has an efficiency of 96.2% at nominal load and at low part-load there is a sharp drop in efficiency.

In PV–EL II, the PV and EL subsystems remain separated; and are directly connected by cable thus omitting the coupling converter, similar to design (f) from Fig. 1. The operating point is found at the crossing point of the U–I-curves of the subsystems. An electrolysis cell (PEM) operates between 1.5–2.0 V,[58] while the PV module has an output voltage of round about 45 V. In order to approximate the operating points, the voltage of the electrolyser is multiplied by n the number of cells in series to mimic a stack of electrolysis cells connected in series, so that an optimal fit of the PV- and EL-operating points is achieved. The
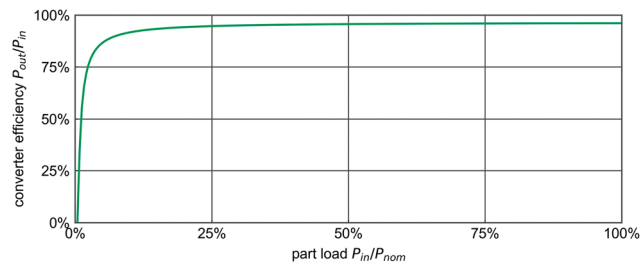

Fig. 6 Part load behaviour of the converter efficiency adapted from the SAM database.[52]
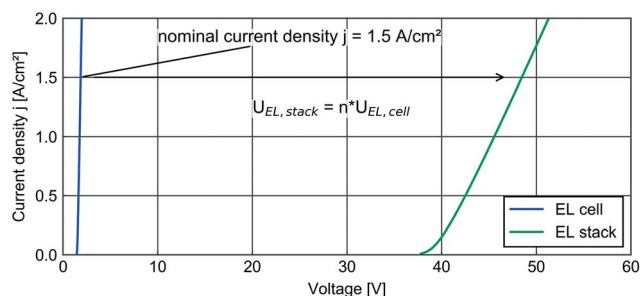

Fig. 7 Exemplary adjustment of the EL-voltage during the design phase from that of a single cell to a stack requiring an input of about 45 V.

adjustment can only be done once, during the design phase. The process is visualised in Fig. 7.

$$V_{EL,stack} = n \times V_{EL,cell} \qquad (11)$$

In reality, the number of cells in series is an integer. Unfortunately, it is hardly possible to match the design point of the electrolysis to a reference output of the PV to 100%.
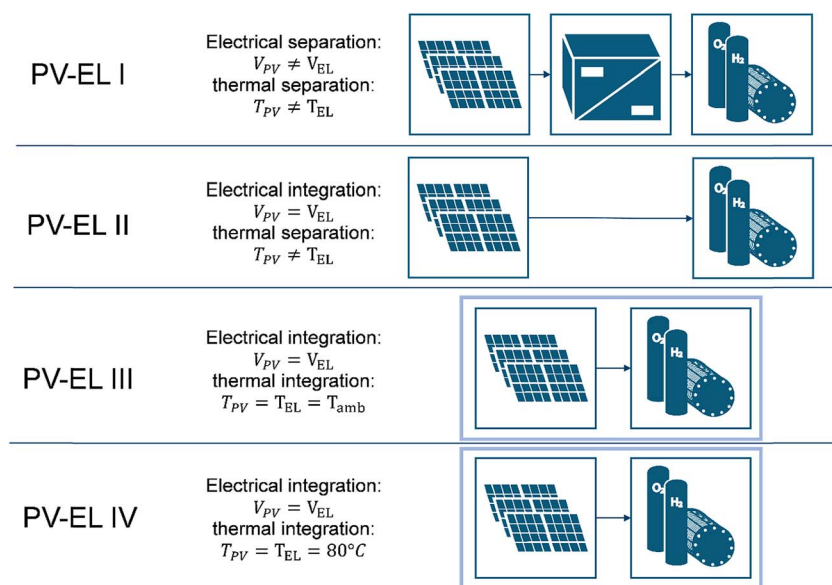

Fig. 5 PV–EL pathways investigated in this study. The arrows in PV–EL I and PV–EL II indicate connecting cables, while for PV–EL III, the two components are monolithically (initimately) connected.

Different reference irradiations for the design of the PV–EL coupling could lead then to arbitrary mismatches of coupling efficiencies between PV and electrolysis and the resulting values would no longer be comparable. Nevertheless, in order to gain insights about the behaviour, especially under varying irradiations and climatic conditions in general, we need comparable results for different pathways and design setups. Therefore, we assumed that the setup has a floating number for the number of EL cells in series. This assumption enables qualitative and comparable insights into the mechanisms of the coupling process without arbitrary side effects. Although, the final results are consequently not directly connected to real expected values.

The resulting curve crossing of the PV and EL subsystems to determine the common operating point is shown in Fig. 8 for direct and converter coupled pathways. Since the design point of the electrolysis system is the power output of the PV at an irradiance of 1000 W m^{-2}, the EL polarisation curve crosses the PV curve at the MPP of 1000 W m^{-2} so that the power input for electrolysis is the power output of the PV at the MPP. Including a converter would cause slight losses which lead to lower power input in the electrolysis system.

For lower irradiances, this behaviour changes such that the EL curve crosses the PV curve at a voltage below that of the Maximum Power Point (MPP) of the PV module thus deviating from the design point. This results in power losses, as only a part of the maximum PV power output is being harvested. These coupling losses lead to the definition of a coupling efficiency η_c:[61]

$$\eta_c = \frac{P_{OP}}{P_{MPP}} = \frac{J_{OP} \times U_{OP}}{J_{MPP} \times U_{MPP}} \tag{12}$$

PV–EL III integrates the PV and EL subsystems into a theoretical single device similar to design (e) from Fig. 1. The subsystems are directly coupled. However, the consideration of an additional relationship between the temperatures of the PV and electrolysis cells is imperative. For simplification, we assumed, that the temperatures of the PV part and are equal:

$$T_{EL} = T_{PV} = T_{amb} \tag{13}$$

The operating temperature of the PV module T_{PV}, is equal to the operating temperature of the electrolysis T_{EL} and connected to the ambient temperature T_{amb}.

At this point, it must be admitted, that the utilization of commercial devices for the PV–EL III is hardly realizable. However, the focus of this study is the investigation of thermal coupling impacts and not the detailed engineering of PV–EL devices. To analyze the impact of thermal coupling, the results for thermally-coupled systems must be comparable to uncoupled devices. Therefore, we used the same PV and electrolysis cell data as in PV–EL I and PV–EL II.

PV–EL IV as the last pathway is considered as a heated integrated device similar to PV–EL III to investigate the influence on temperature on the coupling effects. This still references configuration (e) from Fig. 1. The temperature is set at 80 °C. The energy demand for keeping the system at 80 °C is not considered in this study.

$$T_{EL} = T_{PV} = 80 \ °C \tag{14}$$

This work only models this four PV–EL hydrogen production pathways, discussed above. Modelling a PEC device necessitates that further assumptions are made and additional data is acquired. The PV subsystem of a PEC device does not consist of a PV module so that the one-diode-model for approximating the PV-output cannot be employed. Within the PEC pathway, the PV compartment typically consists of either a single semiconductor layer such a TiO_2 (ref. 12) or a multi-junction light absorber, built from different semiconductors in order to increase the efficiency of light absorption. Multi-junction cells have an output voltage of 1.5–2.8 V (ref. 28) which exceeds the redox-potential needed for direct water splitting, which is 1.23 V. These cells are directly connected to the catalysts, forming the electrodes for the electrolysis process. In order to describe the equivalent electrical circuit of this assembly, a multi-junction PV-model must be developed to approximate the PV subsystem. Such systems are for example shown by Young et al.,[62] but are not part of this study.

3 Results and discussion

This section describes the modelled hydrogen production pathways PV–EL I–IV. First, the design irradiation of the pathways are analysed, and then in a second step, the influences of the operational parameters are analysed at constant ambient temperatures. In a third step, the model is applied to typical meteorological data[63] of Jülich, Germany, to showcase the capability and draw conclusions.

3.1 Design irradiation

The design irradiation G_{design} needs to be defined to determine a reference output from the PV-module and dimension the active electrode area of the electrolyser A_{EL}. Therefore, A_{EL} is determined, so that the MPP of the PV module equals the nominal operating point of the electrolyser. This causes the design irradiation G_{design} to be proportional to the active electrode area A_{EL}. If A_{EL} is known, the current I of the electrolyser
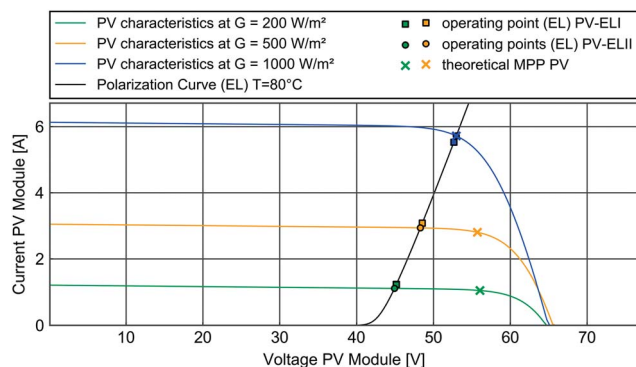

Fig. 8 Determining the operating point represented by symbols at the intersection of the photovoltaic and electrolysis curves (lines). The squares and circles represent the operating points for PV–EL I and PV–EL II, while the cross represents the theoretical maximum power point of the PV module.

can be calculated from the current density j. Two aspects must be considered while choosing this design parameter. On the one hand, a large active electrode area A_{EL} ensures that the electrolyser operates at a low partial load, which causes an increased cell efficiency η_{EL}. This can be derived from eqn (9), given the relationship $\eta_{EL,cell} \sim U_x^{-1}$, with U_x being the operational voltage. On the other hand, a large active electrode area increases the investment costs for the electrolyser subsystem, as the system design must be enlarged and more of the catalyst materials are required. With respect to these aspects, the design of the electrolyser must be adjusted with reference to the local irradiation and hydrogen production pathways.

Fig. 9 depicts the effect of the irradiation on the STH efficiencies of devices using the pathways PV–EL I–IV for various G_{design}. Looking at pathway PV–EL I in Fig. 9, the curves for the different reference irradiations are similar, as they all show the same characteristic progression with increasing irradiation G. Designs for reference irradiations of more then 600 W m^{-2} exhibit a maximum STH efficiency at 200–300 W m^{-2}, followed by a steady decrease as the irradiation further increases. Furthermore, the results reveal a positive correlation of the STH efficiency and G_{design}, as the efficiency increases for designs at higher values of G_{design}. This is explained by processes within the electrolysis subsystem: the high values of the reference irradiation G_{design} correlate with the increased active electrode area allowing the electrolysis cell to operate at lower voltage levels. According to eqn (9), this increases the efficiency of the electrolysis cell in return. The increased electrolysis cell efficiency drives the increase of the STH efficiency as a function of the reference irradiation G_{design}. Meanwhile, since the PV subsystem is independent of G_{design}, for a reference irradiation of 100 W m^{-2}, the voltage of the electrolysis cell would increase above 105% of the nominal PV voltage thus further suppressing the STH efficiency. To address this issue, the

voltage is limited by the power electronics in the converter which reduces the power input into the electrolysis stack. Pathway PV–EL II shows a more complex causality. The peak efficiency for designs at different reference irradiations is found at different irradiations. The irradiation with maximum STH efficiency increases with the reference irradiation. The progression of the curves can be explained by considering the coupling efficiencies. Low reference irradiation causes a large mismatch of the PV operating point and the MPP, resulting in low coupling efficiencies. Without power electronics to adjust the overpotential, the power output drops to zero if the voltage level rises above 105% of the nominal cell voltage.

Pathway PV–EL III shows a similar behaviour compared to PV–EL II, even if the differences of varying G_{design} are smaller compared to PV–EL II. Low values of G_{design} lead to a steep drop in efficiencies with irradiance but the voltage limitation point is not reached. Nevertheless, a design with a reference irradiation of 1000 W m^{-2} exhibits the highest STH efficiency up to irradiances of 900 W m^{-2}.

Since all devices are designed at reference irradiation G_{design} = 1000 W m^{-2}, we take this value as a benchmark henceforth this represents the nominal irradiation for PV modules, it means that the power ratio between electrolysis and PV is 1. However since in practice a value of G = 1000 W m^{-2} is only occasionally reached under real sunlight conditions, the analysis covers a broad range of PV operating conditions.

3.2 Analysis of hydrogen production at constant ambient temperatures

The following investigations will discuss the behaviour of varying irradiances at an ambient temperature of $T = 25\,^{\circ}$C. The reference irradiance G_{design} used to size the system is set to
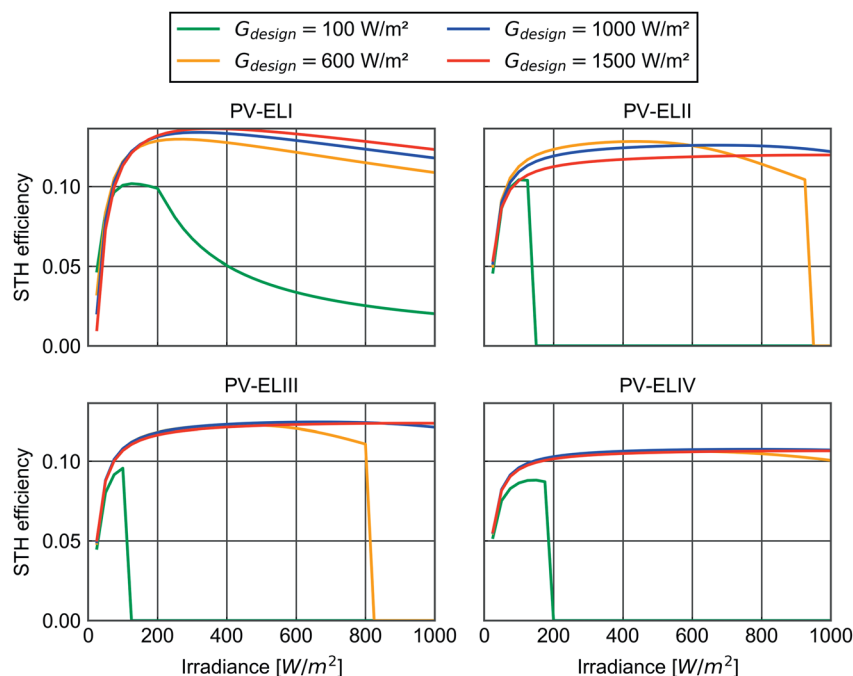

Fig. 9 STH efficiency as a function of the irradiance and designed for different design irradiations G_{design} for systems PV–EL I to IV.

1000 W m^{-2}. The main focus of this section is to determine and compare the hydrogen production *via* the different pathways. The analysis of the overall hydrogen production and the STH efficiencies will be enhanced by a study of the behaviour of the subsystems.

Therefore, Fig. 10 displays the STH efficiencies, the PCE, the efficiency of the electrolysis as well as the coupling efficiency at varying irradiation and constant ambient temperature. The PV–EL I pathway show the highest STH efficiencies within the displayed range of G with its maximum at $G = 325$ W m^{-2}, at a value of 13.4%. The efficiency declines towards higher irradiation levels and reaches an STH efficiency of 11.7% at $G = 1000$ W m^{-2} due to an increasing temperature at the PV module which leads to lower PCE. In addition, the electrolysis efficiency is dropping with rising irradiances due to an increasing voltage level. Pathway PV–EL II reaches efficiencies higher than pathway PV–EL I for irradiations of $G = 700$–1000 W m^{-2} due to the high coupling efficiency at operation close to the design irradiation. At irradiances close to 700 W m^{-2} the STH efficiency of PV–EL II peaks up to 12.5%. The behaviour of pathway PV–EL III results in STH efficiencies slightly below those of PV–EL II for the whole investigated range of G. Thus, two effects are occurring: the thermal integration and connection to T_{amb} causes a drop in electrolysis efficiency due to lower T_{EL}, but an increase of PCE at higher irradiation due to the assumed "cooling" by ambiance. PV–EL IV performs significantly worse than the other pathways, which is caused by the high PV cell temperature and the consequently lower PCE.

Comparing the coupling efficiencies of all investigated pathways, the maximum coupling efficiency for all directly coupled pathways II–IV is 100% at irradiation of $G = 1000$ W m^{-2} since this represents the design point of each pathway. For lower

irradiations, the polarization curve of the electrolyser is not anymore matched with the MPP of the PV module. This voltage drop has the highest influence on the PV–EL II pathway with an efficiency drop down to 83% at 150 W m^{-2}. The coupling efficiency of PV–EL I pathway is linked to the converter efficiency.

3.3 Analysis of hydrogen production in Jülich, Germany

To showcase the models applicability under real sunlight, we applied it on hourly resolved Typical Meteorological Year (TMY) data[63] for global horizontal irradiance as well as the ambient temperature from Jülich, Germany.

Fig. 11 shows exemplarily the hydrogen output per m^2 module area for the first week of July with a reference irradiance of 1000 W m^{-2}. The pathway PV–EL II has slightly higher production at noon, dropping nevertheless below the hydrogen output for PV–EL I during the morning and evening since the STH efficiency benefits occur close to the reference irradiation of 1000 W m^{-2}.

Regarding the results of the whole year, Fig. 12 shows the annual hydrogen production which represents the average STH efficiency as well for all investigated pathways. The pathway PV–EL I has obviously the highest STH efficiency throughout the year, followed by PV–EL II. This means, that the part-load behaviour, in particular, requires further attention when estimating the performance of PV–EL systems since the full load efficiency of an electrically coupled system (PV–EL II) is higher compared to a converter coupled system (PV–EL I). The thermally coupled systems (PV–EL III) linked with the ambient temperature operates close to the PV–EL II system. The higher electrolysis temperatures of a thermal coupling lead to the least efficiency by depressing the PV output.
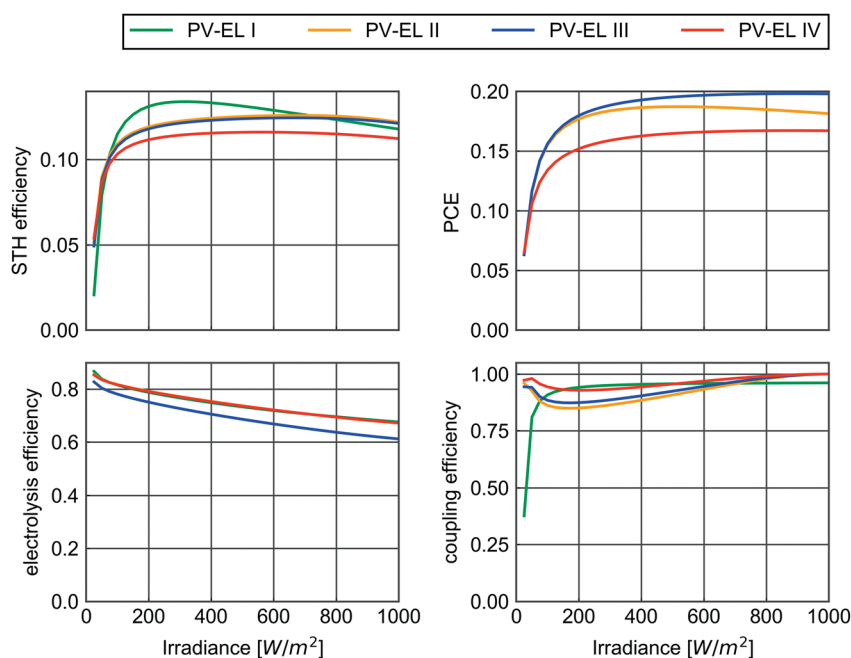

Fig. 10 STH efficiency, PCE, electrolysis efficiency and coupling efficiency of all hydrogen production pathways with component area ratios designed for a design irradiation of 1000 W cm^{-2}.
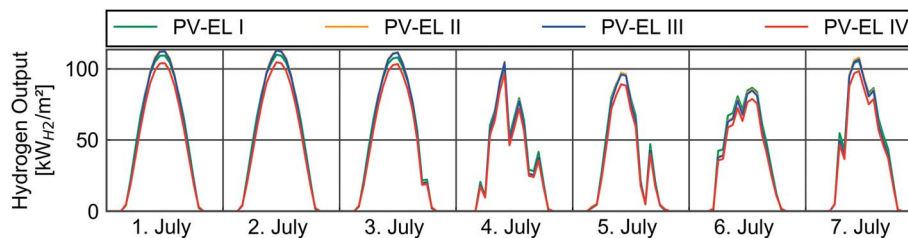
Fig. 11 Hydrogen production of all investigated solar to hydrogen pathways for the first week of July in Jülich based on TMY data[63] with the electrolysis held at 80 °C in all cases except for PV−EL III.
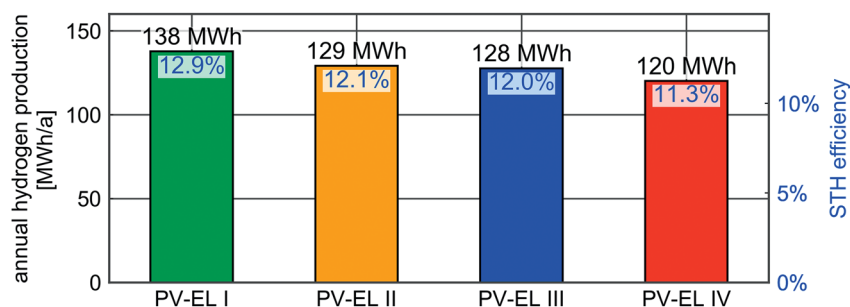

Fig. 12 Annual hydrogen production and average STH efficiencies for all investigated solar hydrogen production pathways in Jülich, Germany, based on TMY data[63] with design irradiance of 1000 W m^{-2} with the electrolysis held at 80 °C in all cases except for PV−EL III.

To get a closer look into the detailed results of the analysis, Fig. 13 shows the STH efficiency against the solar irradiance of each hour in comparison to the STH efficiencies at an ambient temperature of 20 °C corresponding to Fig. 10. There we can see two different results: the STH efficiency for low irradiances of the converter coupled PV–EL I pathway tends to be higher than the expected STH efficiency at an ambient temperature of 20 °C with a rather high spread. The electrically and thermally coupled systems meanwhile show STH efficiencies at real conditions below the design temperature. Nevertheless, there is almost no spread in the STH efficiencies of the directly coupled

systems. This is explained by the PV behaviour at lower ambient temperatures. Lower temperatures mainly increase the open circuit voltage of the PV cell, see Table 1 and Fig. 3. This leads to an increase of the voltage level at the maximum power point while the current remains almost constant. The converter is able to supply the additional power to the electrolysis system. Directly coupled systems are meanwhile not able to adjust this change since the current stays almost constant, the crossing point between PV and electrolysis stays close the crossing point of higher temperatures. The higher theoretical efficiency of the PV is not supplied to the electrolysis system and thus the
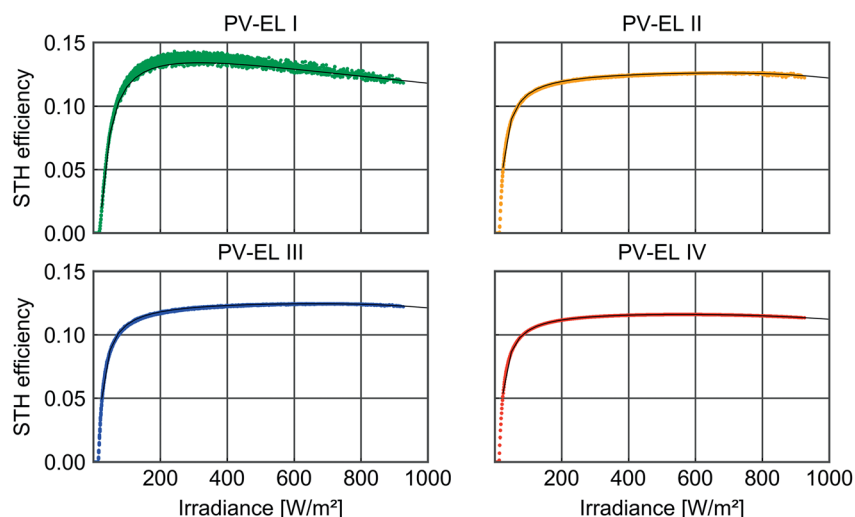

Fig. 13 STH efficiencies at $G_{design} = 1000$ W m^{-2} for Jülich in comparison to the results the analysis at an ambient temperature of 20 °C.
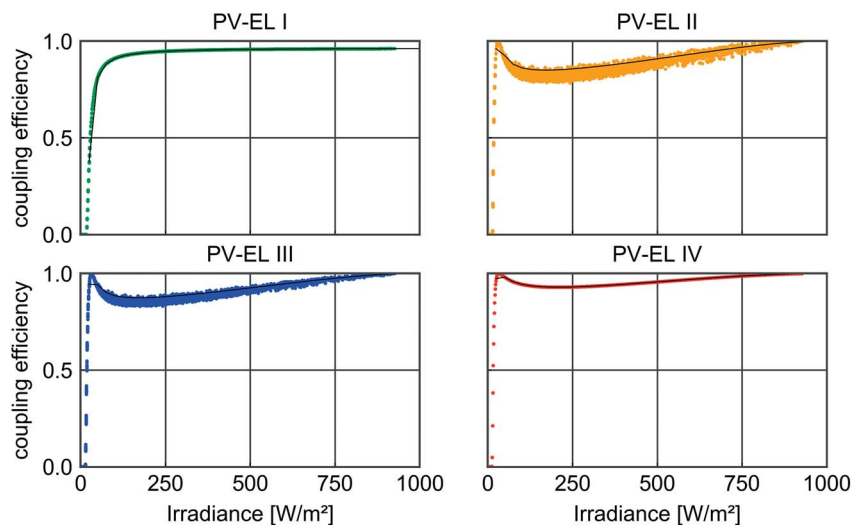
Fig. 14 Coupling efficiencies at $G_{design} = 1000$ W m^{-2} for Jülich in comparison to the results the analysis at an ambient temperature of 20 °C (black line).
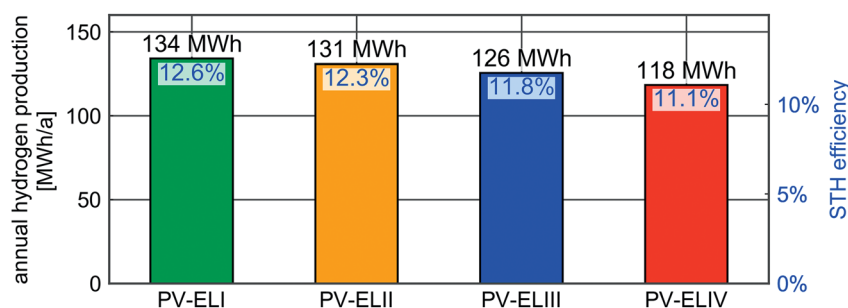

Fig. 15 Annual hydrogen production and average STH efficiencies for all investigated solar hydrogen production pathways in Jülich with design irradiance of 700 W m^{-2} an ambient temperature of 20 °C for the investigated pathways with the electrolyte held at 80 °C in all cases except for PV–EL III.

coupling efficiency drops. This is supported by Fig. 14, which shows that the coupling efficiencies of the directly coupled pathways PV–EL II and PV–EL III drop at lower irradiances below the design efficiency at an ambient temperature of 20 °C.

As a last sensitivity analysis of this study, we changed the design irradiance to 700 W m^{-2}. This would represent a power ratio from the nominal capacity of the electrolysis to the nominal capacity of the PV module of 70% and lead to cheaper costs of the electrolysis. Fig. 15 visualises the resulting annual production. The most interesting part is that PV–EL II produces more hydrogen at lower electrolysis nominal power compared to a design irradiance of 100 W m^{-2} from Fig. 12. The explanation is given by Fig. 9 and the weather data from Jülich: most hours have irradiances of below 700 W m^{-2}. At these irradiances, a G_{design} of 700 W m^{-2} leads to higher efficiencies compared to a G_{design} of 1000 W m^{-2} for PV–EL II while all other pathways become less efficient.

4 Summary and conclusions

The model that is outlined in this work constitutes a possibility for approximating the hydrogen production of multiple solar-to-

hydrogen pathways. A bottom-up approach for determining the hydrogen production was developed, by incorporating the analysis of the subsystems and their interaction, instead of predicting the STH efficiencies on the basis of literature research and experience. This complements the practical construction of solar-to-hydrogen devices in laboratories on the one hand and the top-down and bottom-up modelling approaches of past research on the other. The model builds four different PV–EL pathways, each consisting of a photovoltaic and an electrolysis subsystem. The pathways vary in the degree to which they locally integrate the subsystems into a single device and in the type of electrical connection. PV–EL I separates the subsystems and connects them *via* a converter while PV–EL II separates the subsystems and connects the PV output directly with the EL subsystem. PV–EL III integrates the subsystems into a single device and directly connects them, analogously to PV–EL II. The PV–EL III and IV pathways are in addition coupled thermally at varying operating temperatures.

We showed, that the direct-coupled system PV–EL II is capable of achieving higher efficiencies than the converter-coupled PV–EL I pathway, but only at weather conditions

close to the design point of the system. Varying real-world weather conditions have less influence on a system working with power-electronics (PV–EL I) compared to a directly coupled system (PV–EL II). Thus, precise and careful design of directly coupled system gets more important and consequently more complex. This could be an important key regarding up-scaling and mass-production since the design of coupled systems has to be customised for each production location in worst-case. This could be a major drawback to this technology and will be addressed in future work.

The thermal coupling in PV–EL III and IV showed that an overall efficiency decrease compared to two separated devices for PV and electrolysis because the PV system and the electrolysis work better at low and high temperatures, respectively. A thermally coupling precludes the ability to operate both systems at optimal operational conditions, which is a drawback for the thermal coupled system. Similarities will arise for a PEC device as well. This issue will be a challenge for the development and competitiveness of PEC devices.

The case study on Jülich, Germany, TMY data showed significant deviations in average efficiencies for direct-coupled and converter-coupled systems with benefits for the power electronics. Nevertheless, this paper just addressed the technological background without having a closer look to the economics of all systems. This will have additional influence on the design parameters as well as the different pathways and will be part of future work.

All in all, integrated systems for hydrogen production from PV and electrolysis could offer a solution for cost-efficient systems by omitting power electronics. Nevertheless, an increasing degree of integration comes in line with additional optimisation demand for real-world applications. Therefore, separated devices offer by far more flexibility. An increased integration of subsystem targets for lower hydrogen production costs due to less material usage and demand for peripheral equipment compared to separated devices. In contrast, the decreasing periphery lowers the flexibility of the system's operation. The main question that remains, therefore, is if the loss in flexibility can outweight the saved costs of the periphery.

Nomenclature

a	Modified ideality factor
A_{EL}	Active electrode area of the electrolyser
AM	Air mass
e	Elementary charge
EL	Electrolysis
G	Solar irradiation
G_{design}	Design irradiance
HER	Hydrogen evolution reaction
I_0	Diode reverse saturation current
I_{MPP}	Current at MPP
I_{ph}	Photo current
I_{SC}	Short circuit current
J_{nom}	Current density at nominal operating point of electrolyser

LCOE	Levelised cost of energy
NREL	National renewable energy laboratory
OER	Oxygen evolution reaction
PEC	Photoelectrolysis
PEM	Polymer electrolyte membrane
Pt	Platinum
P_{MPP}	Power at MPP
PV	Photovoltaic
PV–EL	Coupled photovoltaic–electrolysis system
U_{MPP}	Voltage at MPP
U_{nom}	Voltage at nominal operation point of electrolyser
U_{OC}	Open circuit voltage
R_P	Shunt resistance
R_S	Series resistance
SAM	System advisor module
SHJ	Silicon heterojunction technology
STH	Solar-to-hydrogen efficiency
T_{amb}	Ambient temperature
T_{EL}	Electrolysis temperature
T_{PV}	Cell temperature of the PV subsystem
T_{OP}	Operating temperature of the electrolyte
TiO_2	Titanium dioxide
η	Efficiency

Conflicts of interest

There are no conflicts of interest to be declared.

Acknowledgements

References

1 N. Armaroli and V. Balzani, *Angew. Chem., Int. Ed.*, 2007, **46**, 52–66.

2 IEA, *Technology Roadmap Hydrogen and Fuel Cells*, 2015.

3 S. Schiebahn, T. Grube, M. Robinius, V. Tietze, B. Kumar and D. Stolten, *Int. J. Hydrogen Energy*, 2015, **40**, 4285–4294.

4 A. Varone and M. Ferrari, *Renewable Sustainable Energy Rev.*, 2015, **45**, 207–218.

5 M. Götz, J. Lefebvre, F. Mörs, A. McDaniel Koch, F. Graf, S. Bajohr, R. Reimert and T. Kolb, *Renewable Energy*, 2016, **85**, 1371–1390.

6 M. Robinius, A. Otto, K. Syranidis, D. S. Ryberg, P. Heuser, L. Welder, T. Grube, P. Markewitz, V. Tietze and D. Stolten, *Energies*, 2017, **10**, 957.

7 T. Veziroglu and F. Barbir, *Environ. Conserv.*, 1991, **18**(4), 304–312.

8 G. N. Baum, B. D. James, J. Perez and K. N. Baum, *Techno-economic analysis of PEC technologies*, 2009.

9 P. A. Pilavachi, A. I. Chatzipanagi and A. I. Spyropoulou, *Int. J. Hydrogen Energy*, 2009, **34**, 5294–5303.

10 O. Atlam, F. Barbir and D. Bezmalinovic, *Int. J. Hydrogen Energy*, 2011, **36**, 7012–7018.

11 T. J. Jacobsson, V. Fjallstrom, M. Edoff and T. Edvinsson, *Energy Environ. Sci.*, 2014, **7**, 2056–2070.

12 A. Fujishima and K. Honda, *Nature*, 1972, **238**, 37–38.

13 Y. Huang, Y. F. Yu, Y. N. Xin, N. N. Meng, Y. Yu and B. Zhang, *Sci. China Mater.*, 2017, **60**, 193–207.

14 K.-H. Ye, Z. Wang, J. Gu, S. Xiao, Y. Yuan, Y. Zhu, Y. Zhang, W. Mai and S. Yang, *Energy Environ. Sci.*, 2017, **10**, 772–779.

15 S. Wang, L. Zhang, X. Li, C. Li, R. Zhang, Y. Zhang and H. Zhu, *Nano Res.*, 2016, **10**, 415–425.

16 P.-S. Li and H. Teng, *J. Chin. Inst. Chem. Eng.*, 2007, **38**, 267–273.

17 R. Bashiri, N. M. Mohamed, C. Fai Kait, S. Sufian and M. Khatani, *Int. J. Hydrogen Energy*, 2017, **42**, 9553–9566.

18 M. Choi, J. H. Lee, Y. J. Jang, D. Kim, J. S. Lee, H. M. Jang and K. Yong, *Sci. Rep.*, 2016, **6**, 36099.

19 N. Vinothkumar and M. De, *Mater. Renew. Sustain. Energ.*, 2014, **3**(2), DOI: 10.1007/s40243-014-0025-6.

20 D. J. R. Gutiérrez, N. R. Mathews and S. S. Martínez, *J. Photochem. Photobiol., A*, 2013, **262**, 57–63.

21 C. Ding, W. Qin, N. Wang, G. Liu, Z. Wang, P. Yan, J. Shi and C. Li, *Phys. Chem. Chem. Phys.*, 2014, **16**, 15608–15614.

22 Z. Liu, C. Ma, Q. Cai, T. Hong, K. Guo and L. Yan, *Sol. Energy Mater. Sol. Cells*, 2017, **161**, 46–51.

23 H. Cui, W. Zhao, C. Yang, H. Yin, T. Lin, Y. Shan, Y. Xie, H. Gu and F. Huang, *J. Mater. Chem. A*, 2014, **2**, 8612.

24 A. Chatzitakis, A. Papaderakis, N. Karanasios, J. Georgieva, E. Pavlidou, G. Litsardakis, I. Poulios and S. Sotiropoulos, *Catal. Today*, 2017, **280**, 14–20.

25 M. G. Kibria and Z. Mi, *J. Mater. Chem. A*, 2016, **4**, 2801–2820.

26 M. M. May, H. J. Lewerenz, D. Lackner, F. Dimroth and T. Hannappel, *Nat. Commun.*, 2015, **6**, 8286.

27 J. S. Luo, J. H. Im, M. T. Mayer, M. Schreier, M. K. Nazeeruddin, N. G. Park, S. D. Tilley, H. J. Fan and M. Gratzel, *Science*, 2014, **345**, 1593–1596.

28 F. Urbain, V. Smirnov, J. P. Becker, A. Lambertz, F. Yang, J. Ziegler, B. Kaiser, W. Jaegermann, U. Rau and F. Finger, *Energy Environ. Sci.*, 2016, **9**, 145–154.

29 B. Turan, J. P. Becker, F. Urbain, F. Finger, U. Rau and S. Haas, *Nat. Commun.*, 2016, **7**, 12681.

30 G. Heremans, C. Trompoukis, N. Daems, T. Bosserez, I. F. J. Vankelecom, J. A. Martens and J. Rongé, *Sustainable Energy Fuels*, 2017, **1**, 2061–2065.

31 G. Peharz, F. Dimroth and U. Wittstadt, *Int. J. Hydrogen Energy*, 2007, **32**, 3248–3252.

32 S. Licht, B. Wang, S. Mukerji, T. Soga, M. Umeno and H. Tributsch, *J. Phys. Chem. B*, 2000, **104**, 8920–8924.

33 J. Jia, L. C. Seitz, J. D. Benck, Y. Huo, Y. Chen, J. W. Ng, T. Bilir, J. S. Harris and T. F. Jaramillo, *Nat. Commun.*, 2016, **7**, 13237.

34 F. Dimroth, M. Grave, P. Beutel, U. Fiedeler, C. Karcher, T. N. D. Tibbits, E. Oliva, G. Siefer, M. Schachtner, A. Wekkeli, A. W. Bett, R. Krause, M. Piccin, N. Blanc, C. Drazek, E. Guiot, B. Ghyselen, T. Salvetat, A. Tauzin, T. Signamarcheix, A. Dobrich, T. Hannappel and K. Schwarzburg, *Prog. Photovoltaics Res. Appl.*, 2014, **22**, 277–282.

35 S. Kirner, P. Bogdanoff, B. Stannowski, R. van de Krol, B. Rech and R. Schlatmann, *Int. J. Hydrogen Energy*, 2016, **41**, 20823–20831.

36 M. Dumortier and S. Haussener, *Energy Environ. Sci.*, 2015, **8**, 3069–3082.

37 M. Dumortier, S. Tembhurne and S. Haussener, *Energy Environ. Sci.*, 2015, **8**, 3614–3628.

38 A. Maroufmashat, F. Sayedin and S. S. Khavas, *Int. J. Hydrogen Energy*, 2014, **39**, 18743–18757.

39 L. G. Arriaga, W. Martínez, U. Cano and H. Blud, *Int. J. Hydrogen Energy*, 2007, **32**, 2247–2252.

40 B. Paul and J. Andrews, *Int. J. Hydrogen Energy*, 2008, **33**, 490–498.

41 K. Zhou, *Int. J. Hydrogen Energy*, 2008, **33**, 477–489.

42 R. E. Clarke, S. Giddey, F. T. Ciacchi, S. P. S. Badwal, B. Paul and J. Andrews, *Int. J. Hydrogen Energy*, 2009, **34**, 2531–2542.

43 Z. Su, S. Ding, Z. Gan and X. Yang, *Int. J. Hydrogen Energy*, 2014, **39**, 7202–7215.

44 M. R. Shaner, H. A. Atwater, N. S. Lewis and E. W. McFarland, *Energy Environ. Sci.*, 2016, **9**, 2354–2371.

45 R. Sathre, J. B. Greenblatt, K. Walczak, I. D. Sharp, J. C. Stevens, J. W. Ager and F. A. Houle, *Energy Environ. Sci.*, 2016, **9**, 803–819.

46 B. A. Pinaud, J. D. Benck, L. C. Seitz, A. J. Forman, Z. Chen, T. G. Deutsch, B. D. James, K. N. Baum, G. N. Baum, S. Ardo, H. Wang, E. Miller and T. F. Jaramillo, *Energy Environ. Sci.*, 2013, **6**, 1983.

47 R. Garcia-Valverde, N. Espinosa and A. Urbina, *Int. J. Hydrogen Energy*, 2011, **36**, 10574–10586.

48 R. Garcia-Valverde, C. Miguel, R. Martinez-Bejar and A. Urbina, *Int. J. Hydrogen Energy*, 2008, **33**, 5352–5362.

49 F. Sayedin, A. Maroufmashat, S. Al-Adwani, S. S. Khavas, A. Elkamel and M. Fowler, presented in part at the *2015 International Conference on Industrial Engineering and Operations Management*, Ieom, 2015.

50 F. Sayedin, A. Maroufmashat, R. Roshandel and S. S. Khavas, *Int. J. Sustain. Energy*, 2016, **35**, 566–582.

51 F. Sayedin, A. Maroufmashat, S. Sattari, A. Elkamel and M. Fowler, *Energy Convers. Manage.*, 2016, **118**, 438–449.

52 NREL, *System Advisor Model (SAM)*, https://sam.nrel.gov/, 2017.

53 K. Yoshikawa, W. Yoshida, T. Irie, H. Kawasaki, K. Konishi, H. Ishibashi, T. Asatani, D. Adachi, M. Kanematsu, H. Uzu and K. Yamamoto, *Sol. Energy Mater. Sol. Cells*, 2017, **173**, 37–42.

54 Kaneka Corporation, *World's Highest Conversion Efficiency of 26.33% Achieved in a Crystalline Silicon Solar Cell*, http://www.kaneka.co.jp/en/service/news/nr201708252/.

55 V. Tamrakar, S. C. Gupta and Y. Sawle, *Int. J. Electr. Comput. Eng.*, 2015, **4**, 67–77.

56 W. De Soto, S. A. Klein and W. A. Beckman, *Sol. Energy*, 2006, **80**, 78–88.

57 G. Tjarks, *PEM-Elektrolyse-Systeme zur Anwendung in Power-to-Gas Anlagen*, RWTH Aachen, 2017.

58 G. Tjarks, A. Gibelhaus, F. Lanzerath, M. Müller, A. Bardow and D. Stolten, *Appl. Energy*, 2018, **218**, 192–198.

59 D. Stolten, B. Emonts, T. Bergholz, M. Carmo, D. L. Fritz, J.-F. Hake, C. Korte, J. Linssen, S. Luhr, T. Mandt, J. Mergel, R. Peters, V. Tietze, G. Tjarks, J. Wackerl and P. Wasserscheid, *Hydrogen science and engineering : materials, processes, systems and technology*, Wiley-VCH, Weinheim, 2015.

60 F. Barbir, *Solar Energy*, 2005, **78**, 661–669.

61 S. Nordmann, B. Berghoff, A. Hessel, N. Wilck, B. Osullivan, M. Debucquoy, J. John, S. Starschich and J. Knoch, *Renewable Energy*, 2016, **94**, 90–95.

62 J. L. Young, M. A. Steiner, H. Döscher, R. M. France, J. A. Turner and T. G. Deutsch, *Nat. Energy*, 2017, **2**, 17028.

63 European Commission and Joint Research Centre (JRC), *Typical Meteorological Year Data*, https://data.europa.eu/euodp/en/data/dataset/jrc-tmy-tmy-download-service.